JAERI-Research
2000-053

NUMERICAL ANALYSIS OF OPTIMUM ECCD FOR LOCALIZED DRIVEN CURRENT PROFILE IN A TOKAMAK PLASMA

November 2000

Kiyotaka HAMAMATSU and Atsushi FUKUYAMA*

日本原子力研究所
Japan Atomic Energy Research Institute

本レポートは、日本原子力研究所が不定期に公刊している研究報告書です。
入手の問合わせは、日本原子力研究所研究情報部研究情報課（〒319-1195　茨城県那珂郡東海村）あて、お申し越し下さい。なお、このほかに財団法人原子力弘済会資料センター（〒319-1195　茨城県那珂郡東海村日本原子力研究所内）で複写による実費頒布を行っております。

This report is issued irregularly.
Inquiries about availability of the reports should be addressed to Research Information Division, Department of Intellectual Resources, Japan Atomic Energy Research Institute, Tokai-mura, Naka-gun, Ibaraki-ken 〒319-1195, Japan.

編集兼発行　日本原子力研究所

JAERI−Research 2000−053

Numerical Analysis of Optimum ECCD for Localized Driven Current Profile in a Tokamak Plasma

Kiyotaka HAMAMATSU and Atsushi FUKUYAMA*

Department of Fusion Plasma Research
Naka Fusion Research Establishment
Japan Atomic Energy Research Institute
Naka-machi, Naka-gun, Ibaraki-ken

(Received October 4, 2000)

The optimum launching condition of electron cyclotron wave for a localized driven current profile at a targeted magnetic surface is obtained by numerical analysis, where the fundamental O-mode wave is launched in the low field side. The wave launching condition is determined by the direction and position of beam injection and the wave frequency. First the optimum direction of the wave launched at the midplane is analyzed by scanning the launching direction in both the toroidal and poloidal directions. Doppler broadening of the current profile is significantly suppressed, when the current is driven at the position where a ray trajectory becomes tangent to the magnetic surface (referred to as the "tangential resonance"). Second the dependence of the current driven through the tangential resonance on both the location of beam injection and the wave frequency is also examined. It is found that the optimum position is at $60 \sim 70°$ above the midplane and the optimum frequency is in the range of 170∼190GHz for a toroidal magnetic field of 5.5T. It is also shown that the dependence of the tangential resonance condition on the electron temperature is weak.

Keywords: ECCD, O-mode, Numerical Analysis, Tangential resonance, Doppler Broadening, Optimum Injection

* Kyoto University

トカマクにおける局所電流駆動のための最適化されたECCDの数値解析

日本原子力研究所那珂研究所炉心プラズマ研究部
濱松 清隆・福山 淳*

(2000年10月4日 受理)

標的磁気面に局在する電流を駆動するための最適化された電子サイクロトロン波の入射条件を数値解析により求めた。ここでは、O-モード基本波が低磁場側から入射される場合を解析した。波動入射条件は波動の入射方向と入射位置そして周波数により決定される。最初に、赤道面から入射される波の入射方向をトロイダル方向とポロイダル方向の両方向にスキャンして最適入射方向を解析した。光線が磁気面と接する位置で電流が駆動される(「接線共鳴」と参照する)時、ドップラー効果による電流の広がりが著しく抑制される。次に、ビーム入射位置と波動周波数に対する、接線共鳴による駆動電流の依存性を解析した。最適な入射位置は赤道面上の60～70°の位置にあり、波動周波数は5.5Tのトロイダル磁場に対して170~190GHzの周波数帯にあることが示された。更に、電子温度に対する接線共鳴入射条件の依存性は弱いことが示された。

那珂研究所：〒311-0193 茨城県那珂郡那珂町向山801-1
* 京都大学

Contents

目次

This is a blank page.

1. Introduction

The current drive by electron cyclotron (EC) waves is considered as one of efficient methods for steady state operation in a tokamak plasma. The advantages of EC current drive (ECCD) are possibility of localized profile of driven current, controllability of location of driven current, and so on. These properties are very attractive for stabilization of magneto-hydrodynamic(MHD) perturbations, especially the neoclassical tearing mode. In recent years, neo-classical tearing modes have attracted much attentions as an origin of a serious problem which limits the stored energy and deteriorates the confinement.

Many studies concerned with the stabilization of the neo-classical tearing modes have been reported, where ECCD is applied to act on the stability on the plasma. Two methods have been proposed to stabilize the tearing mode by ECCD. The first one is to drive direct current around the magnetic island. To stabilize the MHD perturbations, it is not necessary to maximize the total driven current I, but rather the quantity I/ρ_{w}^2, when the radial width of the driven current ρ_{w} is larger than the island width. The second one is to drive phased current inside the magnetic island, where maximization of I/ρ_{w} is an important issue. Both methods simultaneously require large total current and narrow current profile for efficient stabilization. In the many cases, the injection angle of the ECCD power is so chosen as to deviate by relatively small angle from the perpendicular plane to the magnetic field i.e., small refractive index parallel to the magnetic field $N_{||}$, because the power absorption profile is broadened by Doppler effects for large $N_{||}$. The total driven current, however, may be reduced from the maximum value which can be obtained under the considered situation. The Doppler broadening of the driven current is caused by the power absorption distributed along the ray trajectory crossing the magnetic surfaces. Our attention focuses on the effects caused by the geometrical relation between a ray trajectory and a magnetic surface. It has been shown that the maximum current density is obtained when the ray is tangent to the magnetic surface exactly at the position of wave absorption[5].

In this report, by scanning the direction of beam injection in both the toroidal and poloidal directions, the optimum injection angles are numerically obtained to drive a current with a maximum I/ρ_{w} at the targeted magnetic surface. We analyze the effects of Doppler broadening on the driven current profile. Furthermore, the dependence of driven current on the wave frequency and launching position is examined. This problem has not been fully investigated so far, so that the systematic study is the motivation for the present work. In order to specify the problem, the current driven by the fundamental resonance of the ordinary mode (O-mode) wave is examined for the parameters of a tokamak like the International Thermonuclear Experimental Reactor(ITER). The ray trajectories are calculated by the standard method of geometrical optics [6] and the driven current is calculated by using the adjoint equation for the relativistic Fokker-Planck equation[5]

with the full relativistic Coulomb collision operator[7]. This numerical method enables us to examine a huge number of conditions of wave launching. This paper is organized as follows. In the next section, the numerical model and geometry are explained. The results of numerical analysis are shown in Section 3. In Section 4, summary and discussions are presented.

2. Basic Equation and Numerical Procedure

The EC driven current is obtained by analysis of wave propagation and of deformation of electron velocity distribution. The wave propagation is analyzed by the standard ray tracing method[6]. The ray trajectory is computed by using the Hermitian part of the plasma dispersion tensor with a cold plasma approximation. The wave damping rate is evaluated by numerical integration of the anti-Hermitian part of relativistic dispersion tensor for a plasma with Maxwellian velocity distribution[8]. To compute the driven current, we analyze the linearized Fokker-Planck (F.P.) equation by using the method of adjoint equation[5, 9] in order to save a computation time. Here the deformation of electron velocity distribution function $f_{\rm e1}$ is assumed to be small compared with the Maxwellian distribution $f_{\rm em}$. The linearized Fokker-Planck equation is written as

$$\frac{u_{||}}{\gamma}\frac{B_{\rm p}}{B}\frac{\partial f_{\rm e1}}{\partial \ell_{\rm p}} - C(f_{\rm e1}) = -\nabla \cdot \boldsymbol{S}_{\rm w}, \tag{1}$$

where $u_{||}$ is the electron momentum per unit mass parallel to the magnetic field, γ is the relativistic factor, B is the strength of magnetic field, $B_{\rm p}$ is the poloidal component of magnetic field, and $\ell_{\rm p}$ is the arclength of a field line projected on the poloidal plane. The linearized collision operator $C(f_{\rm e1})$[7] conserves the particle number, momentum and energy for collision between electrons. The wave-induced flux $\boldsymbol{S}_{\rm w}$ is expressed as $\boldsymbol{S}_{\rm w} = -\mathsf{D}_{\rm w} \cdot \nabla f_{\rm em}$, where $\mathsf{D}_{\rm w}$ is the quasi-linear diffusion tensor[5]. When a kind of the Green function $\mathcal{K}$ is introduced by the following adjoint equation:

$$\frac{u_{||}}{\gamma}\frac{B_{\rm p}}{B}\frac{\partial \mathcal{K}}{\partial \ell_{\rm p}} + \frac{C(\mathcal{K} f_{\rm em})}{f_{\rm em}} = -\frac{u_{||}}{\gamma}B, \tag{2}$$

the driven current $\mathcal{J}$ and absorbed power $\mathcal{P}$ are calculated as

$$\mathcal{J} = -\frac{eB}{\langle B^2 \rangle}\left\langle \int d^3u \boldsymbol{S}_{\rm w} \cdot \nabla \mathcal{K} \right\rangle, \tag{3}$$

$$\mathcal{P} = \left\langle \int d^3u \frac{m_e \boldsymbol{u}}{\gamma} \cdot \boldsymbol{S}_{\rm w} \right\rangle, \tag{4}$$

where the operator of magnetic surface average is defined as $\langle A \rangle = (1/V') \oint d\ell_{\rm p} A/B_{\rm p}$ and $V' = \oint d\ell_{\rm p}/B_{\rm p}$. The solution of Eq.(2) in the first order of Legendre expansion can be

expressed by

$$\mathcal{K}(u,\lambda)=\begin{cases}\dfrac{\langle B^2\rangle}{2f_c}\sigma\displaystyle\int_\lambda^{\lambda_c}\frac{d\lambda}{\langle\sqrt{1-\lambda B}\rangle}K(u) & \text{for}\lambda<\lambda_c,\\ 0 & \text{for}\lambda>\lambda_c,\end{cases}\tag{5}$$

where

$$f_c=\frac{3}{4}\langle B^2\rangle\int_0^{\lambda_c}\frac{\lambda d\lambda}{\langle\sqrt{1-\lambda B}\rangle},\tag{6}$$

$\lambda=u_\perp^2/(u_\parallel^2 B)$, $\lambda_c=1/B_{\max}$ and $\sigma=u_\parallel/|u_\parallel|$. The function $K(u)$ is the solution of a one dimensional integro-differential equation:

$$\frac{\partial}{\partial u}\left(u^2D_{uu}\frac{\partial K}{\partial u}\right)-\frac{m_e u}{T_e\gamma}D_{uu}\frac{\partial K}{\partial u}-\left(\frac{2D_{\theta\theta}}{u^2}+\frac{\gamma\Gamma^{e/e}Z_{\rm eff}}{u^3}\right)\frac{K}{f_c}+I^{e/e}[K]-\frac{u}{\gamma}=0,\tag{7}$$

where $Z_{\rm eff}$ is the effective charge number of multi species ions. Eq.(7) with $f_c=1$ is same to the key equation of the relativistic Spitzer-Harm problem[7]. The details of notation in Eq(7) are described in Ref.[7]. The numerical recipe for Eq.(7) is minutely explained in Ref.[10]. From the view point of numerical calculation, it is very important that the a numerical cost for solving the Eq(7) is very low and the function $\mathcal{K}$ does not depend on the properties of EC wave, i.e., $\boldsymbol{S}_{\rm w}$. This enables us to comb the driven current profile localized at the targeted magnetic surface by varying the direction of the beam injection. Though the analysis based on the adjoint equation is limited in the linear approximation, we consider that it is permissible to apply linear analysis to the case of the off-axis current drive owing to the low power density. It is our purpose to examine the Doppler effects on the driven current profile with a maximum $I/\rho_{\rm w}$ within the off-axis region. In this article, the plasma is assumed to be confined by nested magnetic surfaces. And also, it is assumed that a stationary current is sustained by the EC wave. In order to stabilize the tearing modes, however, the phased current must be driven inside the magnetic islands. We will discuss our assumption in the last section.

The configurations and notations used in the numerical calculation are explained in the following. EC waves are traced in cylindrical coordinates (R,φ,z), where the system is assumed to be axially symmetric. The ray trajectory starts from $(R_{\rm i},z_{\rm i})$, which is set just inside the outermost magnetic surface. The location on the magnetic surface is specified by the poloidal angle $\chi_{\rm i}=\tan^{-1}((z_{\rm i}-Z_0)/(R_{\rm i}-R_0))$, where (R_0,Z_0) is the position of the magnetic axis. The direction of beam injection is specified by the toroidal and poloidal injection angles, $\theta_{\rm t}$ and $\theta_{\rm p}$, which correspond to two subsequent rotations: first, in the poloidal plane the direction is rotated out of the horizontal plane, and, second around the vertical axis. The driven current density is expressed as $J(\rho,\theta_{\rm t},\theta_{\rm p})$, where $\rho=\sqrt{V(\psi)/(2\pi^2R_0)}$ and $V(\psi)$ is the volume within the magnetic flux surface ψ. When the position of the driven current, $\hat{\rho}$, is defined by the peak position of the current density,

$\hat{\rho}$ becomes a function of the injection angles θ_t and θ_p. Then the total driven current is expressed as $I = I(\theta_t, \theta_p)$. The width of the driven current is defined as $\rho_w \equiv I/(2\pi\hat{\rho}\hat{J})$, where $\hat{J} = J(\hat{\rho}, \theta_t, \theta_p)$. If $\rho_w/2 > \hat{\rho}$, then the definition is changed to $\rho_w \equiv \sqrt{I/(\pi\hat{J})}$.

To maximize the value of I/ρ_w at the targeted magnetic surface, the direction of wave injection is scanned in the (θ_t, θ_p)-plane. Hereafter the notation $\Upsilon = I/\rho_w$ is used. Then the following numerical procedure is employed. First by seeking the poloidal injection angles θ_p under the condition of fixed $\hat{\rho}$ and θ_t, we can find several (usually one or two) poloidal injection angles. The maximum Υ as a function of $\hat{\rho}$ and θ_t, Υ_p, is determined by picking up the maximum value among the values of Υ with the obtained poloidal injection angles, i.e.;

$$\begin{aligned} \Upsilon_p(\hat{\rho}, \theta_t) &= \max_{\theta_p} \Upsilon(\theta_t, \theta_p) \quad \text{with fixed } \hat{\rho}(\theta_t, \theta_p) \text{ and } \theta_t \\ &= \Upsilon(\theta_t, \bar{\theta}_p), \end{aligned} \tag{8}$$

where $\bar{\theta}_p$ is also a function of $\hat{\rho}$ and θ_t. Second the toroidal injection angle θ_t is varied. The maximum of Υ on the targeted magnetic surface $\hat{\rho}$ is obtained as

$$\Upsilon_{pt}(\hat{\rho}) = \max_{\theta_t} \Upsilon_p(\hat{\rho}, \theta_t) = \Upsilon(\hat{\theta}_t, \hat{\theta}_p) \tag{9}$$

where $\hat{\theta}_t$ is a function of $\hat{\rho}$ and $\hat{\theta}_p = \bar{\theta}_p(\hat{\rho}, \hat{\theta}_t)$. In this report, $\hat{\theta}_t$ and $\hat{\theta}_p$ are called the optimum angles.

3. Numerical Results

It is our purpose to find the optimum launching condition, i.e., the optimum angles and optimum launching position and the optimum wave frequency, with maximum value of Υ at the targeted magnetic surface. First the optimum injection angles for Υ_{pt} are sought without consideration of finite beam size. Next the dependence of the driven current profile on the launching position and wave frequency is analyzed taking the effects of beam divergence and of finite beam width into account.

As for the plasma parameters, we employ a tokamak like ITER-Feat: R_0 =6.20m, a = 1.90m, B_0 =5.51T, I_p =13.3MA, κ =1.60, δ =0.241, n_{e0} =1.17×10^{20}m^{-3}, and T_{e0} =30keV, where the both direction of the toroidal magnetic field and the toroidal plasma current are counterclockwise. The profiles of the density and temperature are the following: $n_e(\psi) = n_{e0} \times (1 - \psi/\psi_s)^{0.15}$ and $T_e(\psi) = T_{e0} \times (1 - \psi/\psi_s)$, where ψ_s means ψ on the plasma boundary. Further a flat Z_{eff} profile is assumed with Z_{eff} = 2. The fundamental O-mode wave is launched from the low field side. In the following numerical analyses, the total input power P_{inp} is fixed to 1MW.

3.1 Optimum Direction of Beam Injection

The currents driven by the waves injected at $\chi_i = 0$ and 70° with a frequency of f =180GHz are examined by the single ray analysis, i.e., effects of finite beam size are not included.

Figure 1 illustrates the dependence of Υ on the injection angles, where the waves are injected at $\chi_i = 0$ and the minor radius is normalized by $\rho_s = \rho(\psi_s) \simeq 2.4$m. In the middle part of the figure, intensity of Υ_p is drawn in the $(\hat{\rho}, \theta_t)$-plane, where the ridge of the intensity plot corresponds to the optimum toroidal angle $\hat{\theta}_t$ indicated by the solid curve. In the upper part of the figure, the solid curve shows Υ_{pt} defined by Eq.(9) and the dotted curve shows Υ_p with θ_t fixed at 31°, which is also indicated by the dotted line in the middle part of the figure. In the lower part of the figure, the optimum poloidal angle $\hat{\theta}_p$ and $\bar{\theta}_p$ with θ_t fixed at 31° are described by the solid and dotted curves, respectively. Many corrugations or spikes appear in these curves, since the injection angles are scanned with the same intervals ($\Delta\theta_t = 0.5°, \Delta\theta_p = 0.25°$) and the driven current density J is evaluated in shells divided by the same width ($\Delta\rho/\rho_s = 0.005$). The optimum angles vary discontinuously at $\hat{\rho}/\rho_s \sim 0.67$.

First the driven current in the region of $\hat{\rho}/\rho_s \lesssim 0.5$ is considered. Figure 2 shows the poloidal projection of typical ray trajectories injected by optimum angles shown in figure 1. The fundamental harmonic resonance layer ($f = f_{ce}$) is also plotted by the dashed

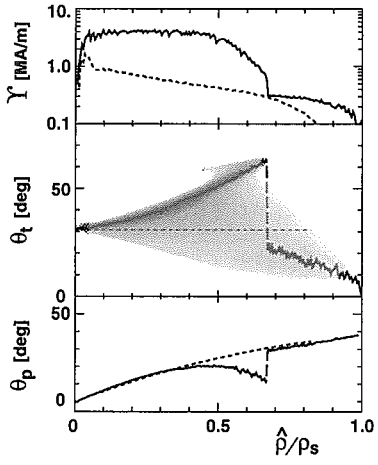

Figure 1. The dependence of Υ on the injection angles in the case of the waves injected at $\chi_i = 0$. In the middle part, intensity of Υ_p is shown in the $(\hat{\rho}, \theta_t)$-plane. The ridge of intensity plot corresponds to the optimum toroidal angle $\hat{\theta}_t$ indicated by the solid curve. In the upper part, the solid curve shows Υ_{pt} defined by Eq.(9) and the dotted curve shows Υ_p with θ_t fixed at 31°, which is also indicated by the dotted line in the middle part. In the lower part, the optimum poloidal angle $\hat{\theta}_p$ and $\bar{\theta}_p$ with θ_t fixed at 31° are described by the solid and dotted curves, respectively.

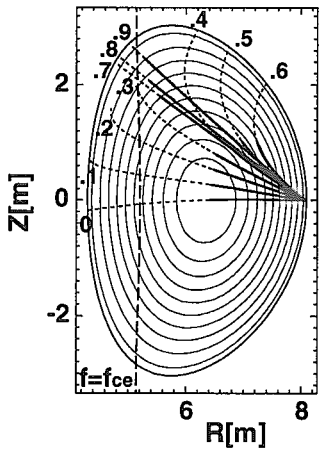

Figure 2. The poloidal projection of typical ray trajectories injected by optimum angles shown in figure 1. The fundamental harmonic resonance layer ($f = f_{ce}$) is also plotted by the dashed curve. When half of the wave energy is absorbed, solid curves are changed to dotted. The peak radius of driven current density, $\hat{\rho}/\rho_s$, are indicated near each ray. The ray trajectories are arbitrarily stopped after the wave power is perfectly absorbed.

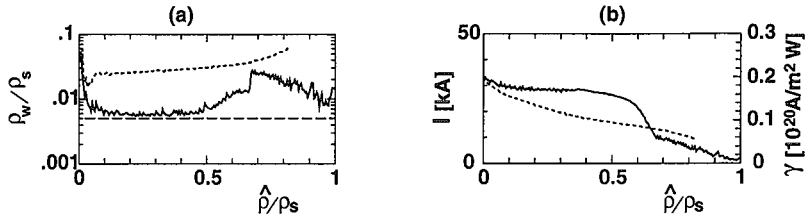

Figure 3. ρ_w and I as functions of $\hat{\rho}$. The solid curve indicates the case of optimum injection and the dotted curve the case with the fixed θ_t shown in the dotted curves in figure 1. In (a), the dashed line shows the radial mesh size.

curve. When half of the wave energy is absorbed, solid curves are changed to dotted ones; the peak radius of driven current density, $\hat{\rho}/\rho_s$, are indicated near each ray. Furthermore the ray trajectories are arbitrarily stopped after the wave power is perfectly absorbed. The position of power absorption is close to the position of the current drive. Here, we note that the current is driven at the position where the ray trajectory becomes tangent to the magnetic surface. We call this type of resonance the "tangential resonance" in real space. With the increase in θ_p, the location of tangential resonance shifts towards the low field side. At the same time, $N_{||}$ is increased by the increase in θ_t shown in figure 1. The power absorption at the tangential resonance point is caused by the enhancement of the Doppler effect. Of course, the power absorption region is broadened along the ray trajectory by the enhancement of the Doppler effect. Figure 3 shows ρ_w and I as a function of $\hat{\rho}$, where the solid curve indicates the case of optimum injection and the dotted curve the case with the fixed θ_t shown in the dotted curves in figure 1. Figure 3 (a) shows that ρ_w for the optimum injection lies close to the radial mesh size shown by dashed line , i.e., $\rho_w/\rho_s \simeq 0.005$. Although the cyclotron resonance region is broadened by the Doppler effect, the radial width of driven current is significantly reduced due to the tangential resonance. On the other hand, ρ_w with θ_t fixed at 31° is broadened by the Doppler effects. In figure 3 (b), as $\hat{\rho}$ increases, the total driven current with a fixed θ_t decreases due to the increase in the collisionality and in the ratio of trapped particles. In the case of the optimum injection, the total driven current is kept around the value of 30kA, because the increase in the driving force caused by the increase in $N_{||}$ is almost cancelled by the increase in the collisionality and in the population of trapped particles. The maximum Υ is achieved by both the increase in I and the decrease in ρ_w. In this figure, the current drive efficiency γ is also shown for reference, where $\gamma = \langle n_e \rangle R_0 I / P_{inp}$ and $\langle n_e \rangle$ is the volume averaged electron density.

In the region of $0.5 \lesssim \hat{\rho}/\rho_s$, Υ_{pt} decreases (see the solid curve in the upper part of figure 1). In figure 2, the ray trajectories on poloidal projection with $0.5 \lesssim \hat{\rho}/\rho_s \leq 0.6$ bend at the tangential resonance position owing to the refraction and the toroidal effect. This bend in the ray trajectory causes the increase in ρ_w (see figure 3(a)) and the decrease in Υ. Furthermore, in the region $0.6 \lesssim \hat{\rho}/\rho_s \lesssim 0.68$, the wave power is not absorbed perfectly at the tangential resonance position because of the large distance from the layer

for $f = f_{ce}$ and of the low electron temperature. Figure 4 shows the absorbed power as a function of $\hat{\rho}$, where the solid curve shows the total absorbed power and the dashed curve shows the absorbed power by the fundamental cyclotron resonance. The rest of the power is absorbed by the down shifted second harmonic resonance. The current is driven by the fundamental resonance power absorption. This figure shows that the total absorbed power decreases in the region of $0.6 \lesssim \hat{\rho}/\rho_s \lesssim 0.68$, where Υ_{pt} still becomes a maximum near the tangential resonance in spite of lost power. When $\hat{\rho}/\rho_s$ becomes larger than about 0.68, however, the injection angles for Υ_{pt} are found in the other branch, where the power is perfectly absorbed, since the power absorbed through the tangential resonance no longer drives sufficient current. On the new branch, the power is absorbed perfectly near the layer where $f = f_{ce}$ by the injection with small $\hat{\theta}_t$. However, we obtain neither large I nor large Υ because of the small $N_{||}$ and power absorption due to the second harmonic resonance.

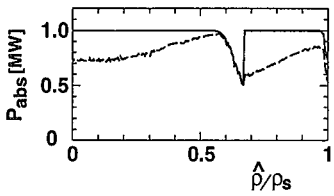

Figure 4. The absorbed power as a function of $\hat{\rho}$. The solid curve shows the total absorbed power and the dashed curve shows the absorbed power by the fundamental cyclotron resonance.

By considering that the current drive through the tangential resonance depends on the relation between the location of beam launching and that of the layer where $f = f_{ce}$, we examine the current drive by a wave injected at $\chi_i = 70°$ with a frequency of $f = 180$GHz. Figures 5 to 8 correspond to figures 1 to 4, respectively. In figure 5, the optimum injection angles jump discontinuously at the position of $\hat{\rho}/\rho_s \sim 0.88$ and Υ_{pt} is low in the region $0.88 \lesssim \hat{\rho}/\rho_s$. Figure 6 and figure 7 show that the current is driven through the tangential

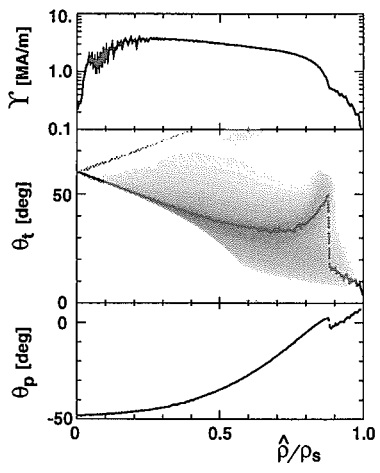

Figure 5. The dependence of Υ on the injection angles in the case of the waves injected at $\chi_i = 70°$. The figure is drawn by the same manner of figure 1 without the dotted line.

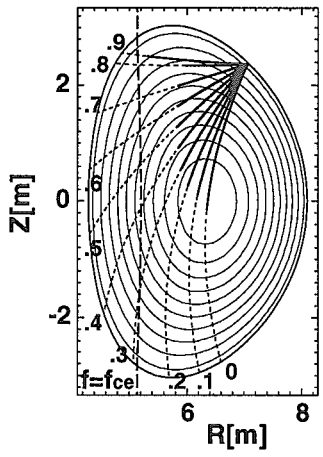

Figure 6. The poloidal projection of typical ray trajectories injected by optimum angles shown in figure 5. The figure is drawn by the same manner of figure 2.

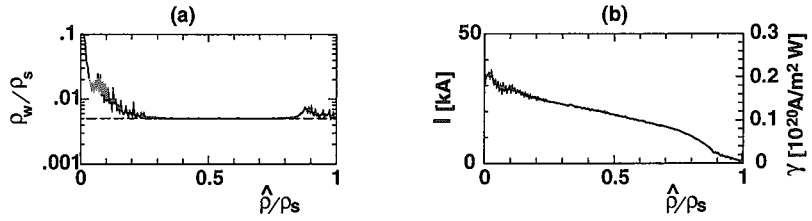

Figure 7. ρ_w and I as functions of $\hat{\rho}$ in the case of the waves injected at $\chi_i = 70°$ The figure is drawn by the same manner of figure 3 without the dotted line.

resonance in the region $\hat{\rho}/\rho_s \lesssim 0.88$. Figure 6 also shows that the tangential resonance positions shift into the high field side where the population of trapped electrons decreases and that the ray trajectories become almost straight compared with figure 2. In figure 7 (a), the current width ρ_w is reduced to the radial mesh size. This is caused by the straight ray trajectory and the reduction of the Doppler effects due to the decrease in $\hat{\theta}_t$, i.e., decrease in $N_{||}$. On the other hand, the total driven current does not increase so much due to the decrease in $N_{||}$. Furthermore, figure 8 shows that the absorbed power does not exhibit a sharp decline around $\hat{\rho}/\rho_s \simeq 0.88$ and that the wave power is perfectly absorbed by the fundamental cyclotron resonance. The optimum direction of beam injection is determined as the result of the competition among the above effects.

Here, it must be noted that the correct value of Υ_{pt} may be lower than the value of Υ_{pt} obtained by the single ray analysis, since the ρ_w is close to the numerical radial mesh size. We can not conclude which launching position is better in this subsection. In this situation, the effects of beam divergence and of finite beam width become essential.

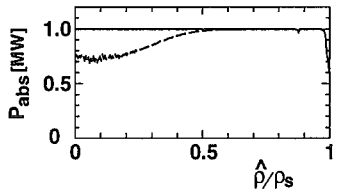

Figure 8. The absorbed power as a function of $\hat{\rho}$ in the case of the waves injected at $\chi_i = 70°$. The figure is drawn by the same manner of figure 4.

3.2 Dependence on Launching Position and Wave Frequency

In the previous subsection, the optimum injection angles are obtained by the single ray analysis. The total driven current is not affected so much by a beam cone with finite size. Single ray analysis only reveals the driven current density profile width as a consequence of the absorption profile broadening that occurs along the propagation of the ray. This leads to the smallest deposition width and possibly the highest Υ for tangential resonance conditions. The effects of divergence and finite spatial width of the wave beam is to broaden the power deposition and the driven current density profile in the direction perpendicular to the propagation of the beam. Consequently, the effects of profile broadening due to finite beam size can be minimized by propagation as close to perpendicular to the magnetic surface as possible. By using the optimum injection angles obtained from the single ray analysis, we examine the dependence of the driven current

profile on the launching position and wave frequency by taking into account the effects of finite beam size.

Here we analyze the beam cone injected by a single waveguide. The beam cone is assumed to be focused at the starting point just inside of the outermost magnetic surface. Furthermore, we assume that the beam cone has a Gaussian power distribution with a full angle of 2°. The effect of finite beam width Δr is also taken into account, where the relation between Δr and expanse of the wave vector Δk is determined by $\Delta k \cdot \Delta r = 2\pi$. This beam cone is simulated by a bundle of 49 rays and the total power is also set at 1MW.

Figure 9 shows contours of Υ_{pt} in the $(\hat{\rho}, f)$-plane, where the frequency and $\hat{\rho}$ are varied with intervals of 10GHz and of 0.1, respectively. The injection position is set at $\chi_i = 0$ and shifted from 50° to 80° with an interval of 10° , which corresponds to figure 9 (a) to (e). The best launching condition is determined by maximizing the current density at the specified radial position and value of Υ_{pt}. In this paper, we look for the wave launching condition to obtain a large value of Υ_{pt} in a range of minor radius as wide as possible. In the case of $\chi_i = 0$ (figure 9(a)), a large value of Υ_{pt} can be obtained only in the core region $\hat{\rho}/\rho_s \lesssim 0.4$. In the case of $\chi_i = 50°$ (figure 9(b)), the radial profile of Υ_{pt} becomes almost a flat peak in the region $0.2 \lesssim \hat{\rho}/\rho_s \lesssim 0.6$ and in the frequency range 170GHz $\lesssim f \lesssim$ 190GHz. However, Υ_{pt} decreases in the region $\hat{\rho}/\rho_s \gtrsim 0.7$. When the EC wave is injected at $\chi_i = 60°$ (figure 9(c)), Υ_{pt} in the region $\hat{\rho}/\rho_s \gtrsim 0.7$ is improved in the frequency range 180GHz $\lesssim f \lesssim$ 190GHz as compared with figure 9(b). Furthermore, the injection at $\chi_i = 70°$ improves Υ_{pt} in the same radial region and in the same frequency

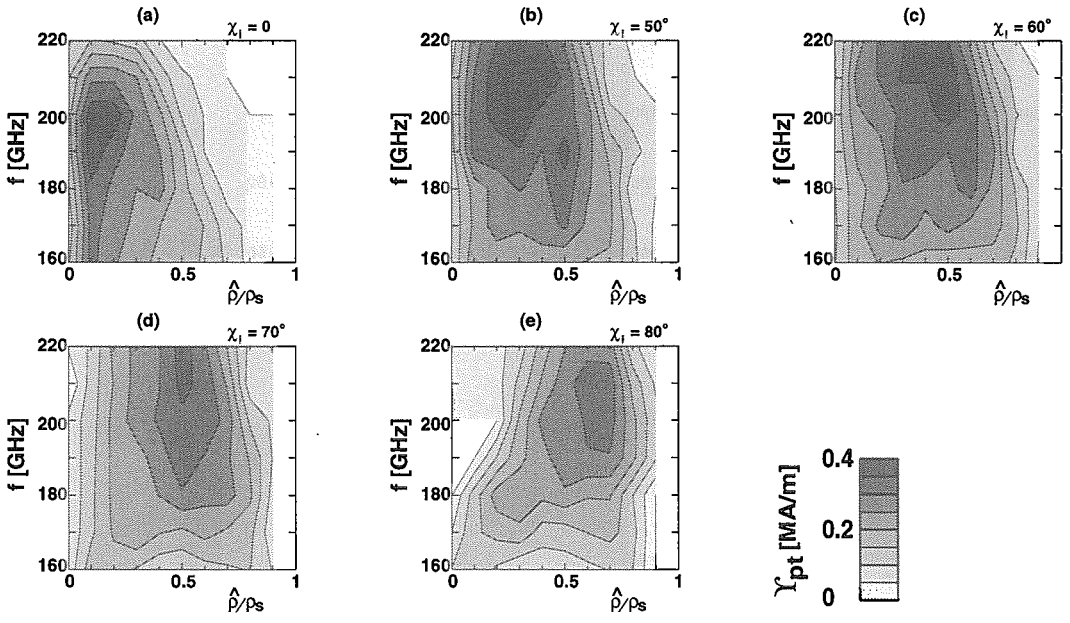

Figure 9. Contours of Υ_{pt} in the $(\hat{\rho}, f)$-plane. The frequency and $\hat{\rho}$ are varied with intervals of 10GHz and of 0.1, respectively. The injection position is set at $\chi_i = 0$ and shifted from 50° to 80° with an interval of 10°, which corresponds to figure 9 (a) to (e).

range. However, the launching at $\chi_i = 80°$ reduces Υ_{pt} in the whole plasma region. In conclusion, the injection at $\chi_i \sim 70°$ with the frequency of $f = 180 \sim 190$GHz is better for driving the current with a large value of Υ_{pt} in the radial region of $0.2 \lesssim \hat{\rho}/\rho_s \lesssim 0.8$. The total driven current I and the driven current width ρ_w are also shown for reference in figure 10 and 11, respectively.

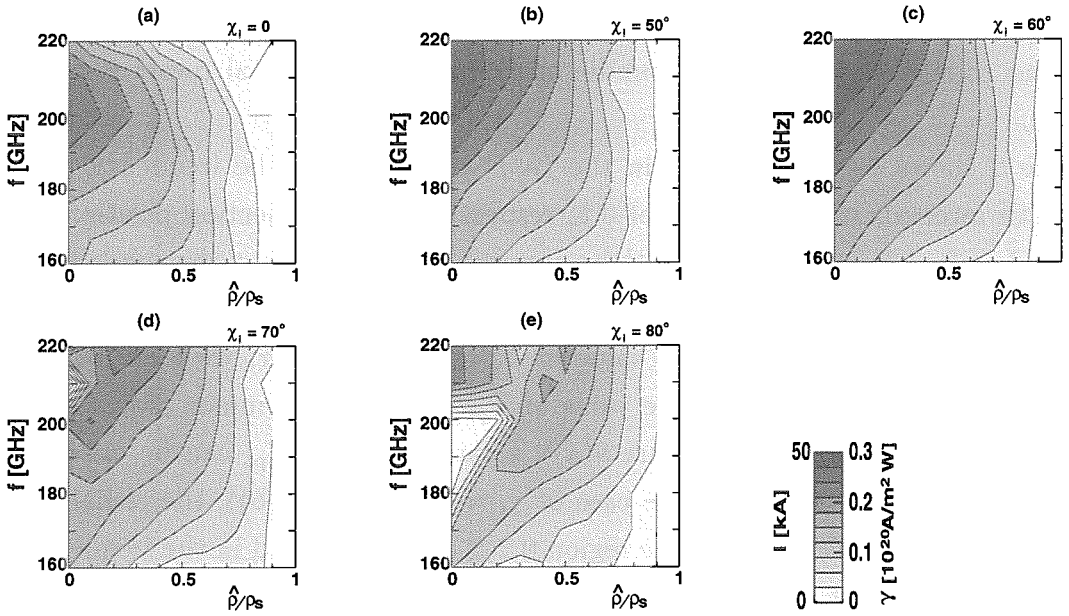

Figure 10. Contours of I in the $(\hat{\rho}, f)$-plane. The figure is drawn by the same manner of figure 9.

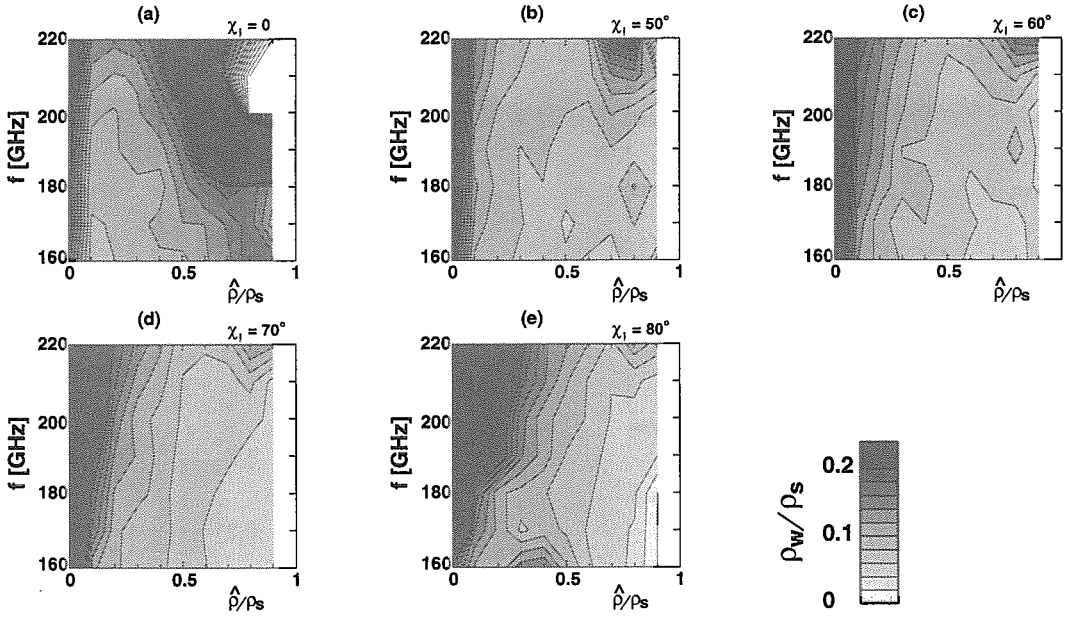

Figure 11. Contours of ρ_w in the $(\hat{\rho}, f)$-plane. The figure is drawn by the same manner of figure 9.

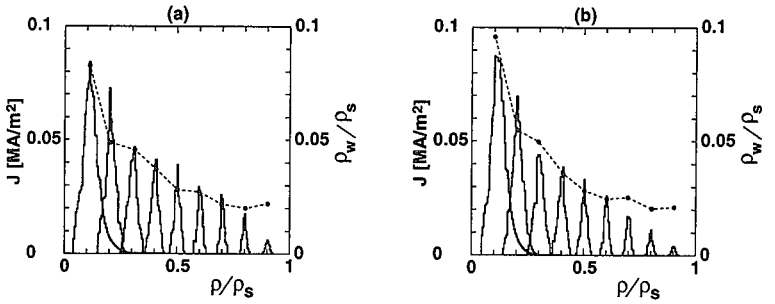

Figure 12. The radial profiles of the driven current. (a) and (b) show the cases of T_{e0} =30keV and 20keV, respectively,

3.3 Dependence on Electron Temperature

The dependence on electron temperature is examined for the current driven by a wave launched at $\chi_i = 70°$ with a frequency of f=180GHz. The radial profiles of the driven current in target plasmas with T_{e0} =30keV and 20keV are illustrated in figure 12 (a) and (b), respectively, where the optimum injection angles are also obtained by the single ray analysis and $\hat{\rho}/\rho_s$ is varied from 0.1 to 0.9 with an interval of 0.1. In the core region, the effects of finite beam size slightly shift the peak positions from $\hat{\rho}$ obtained by the single ray analysis. In so much the wave power is absorbed mainly by the fundamental resonance, this shift is negligible. Here, we note that $\hat{\rho}$ in figures 9 to 11 is evaluated by the single ray analysis. In figure 12, ρ_w is also plotted by solid circles. The current profile is scarcely affected by the electron temperature. The optimum injection angles in the case of T_{e0} = 20keV are illustrated in figure 13. The radial position, where the current driven through the tangential resonance disappears, shifts inward a little. The radial dependence of $\hat{\theta}_t$ and $\hat{\theta}_p$ does not vary so much in the region $\hat{\rho}/\rho_s \lesssim 0.7$ in comparison with the case of T_{e0} = 30keV. Figure 14 illustrates I and Υ_{pt}, where the solid and dotted curves show the cases of T_{e0} =20keV and 30keV, respectively. In figure 14(a), I for T_{e0} =30keV is smaller than that for 20keV in the region $\hat{\rho}/\rho_s \lesssim 0.3$, because of the power absorption by the second harmonic resonance. In the case of T_{e0} =20keV, the power absorbed by the second harmonic resonance is negligible in the whole minor radius. When the wave is injected at the optimum angles, the driven current does not depend so much on the electron temperature.

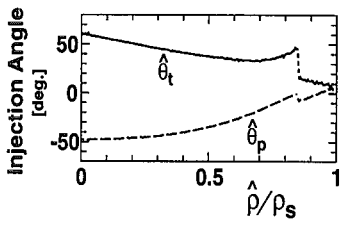

Figure 13. The optimum injection angles in the case of T_{e0} = 20keV.

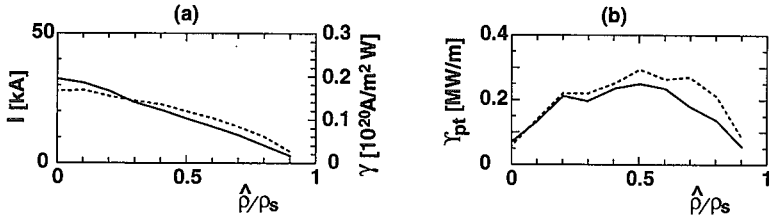

Figure 14. I and Υ_{pt} as functions of $\hat{\rho}$. The solid and dotted curves show the cases of T_{e0} =20keV and 30keV, respectively.

4. Summary and Discussions

The ECCD by the fundamental O-mode has been numerically analyzed. In order to drive the current with the maximum I/ρ_w on the desired magnetic surface, the optimum injection angles have been examined by using the single ray analysis. When the current is driven around the position where a ray trajectory becomes tangent to the magnetic surface, the Doppler broadening of the driven current profile can be significantly suppressed. The radial region where the current is driven through the tangential resonance strongly depends on the beam launching position and wave frequency. Launching from the position off the midplane can drive the current through the tangential resonance in the region $\rho/\rho_s < 0.9$. When the current is driven through the tangential resonance, the driven current profile is mainly broadened by the effects of finite beam size. These effects are analyzed for the optimum injection angle obtained by the single ray analysis. Also, the dependence of I/ρ_w on both the launching position and wave frequency has been obtained. The width of the driven current is kept within 2$\sim$ 5% of the minor radius. It is also shown that the dependence of the optimum injection angles and the driven current on the electron temperature is weak.

In this paper, the plasma is assumed to be confined by nested magnetic surfaces; i.e., the magnetic islands are not taken into account. Also, the optimum injection is discussed for the maximum I/ρ_w, which is used as a parameter for stabilization of the neo-classical tearing mode by using phased current drive within a magnetic island. The numerical results obtained here can not be directly applied to the analysis for stabilization of the neo-classical tearing mode. When one sees the field lines of magnetic island along the toroidal direction, the magnetic field line is gently twisted around the magnetic axis of the island. If the current is driven through the tangential resonance to the magnetic axis of the island, the total amount of driven current may not be affected so much. At the same time, the width of the driven current profile may be broadened by the finite beam size. The driven current density, however, will be strongly dependent on the area surrounded by the magnetic surface. We show that the width of the driven current profile can be controlled in the range 0.05$\sim$0.1m under the assumption of a beam divergence of 2°. On the other hand, the width of the seed island is evaluated to be about .05m[1]. Current drive through the tangential resonance, it is hoped, can reduce the island width to around the seed island width. Of course, a numerical analysis taking into account the island structure and temporal development of the driven current is necessary to confirm the effects of tangential resonance. This analysis is left for future study.

Acknowledgements

One of the authors, K.H., also wish to express thanks to Dr. J Koga for useful discussions and comments.

References

[1] H.Zohm, Phys. Plasmas **4** 3433 (1997)

[2] C.C.Hegna, J.D.Callen, Phys. Plasmas **4**, 2940 (1997).

[3] G.Giruzzi, M.Zabiego, T.A.Gianakon, X.Garbet, A.Cardinali, S.Bernabei, Nucl. Nusion **39** 107 (1999).

[4] ITER Physics Expert Group on Energetic Particles, Heating and Current Drive, Nucl. Fusion **39** 2495 (1999).

[5] K.Hamamatsu, A.Fukuyama, "Controllability of driven-current profile in ECCD on ITER", Fusion Engineering Design [in press].

[6] I.B. Bernstein, Phys.Fluids **18**, 320 (1975).

[7] B.J.Braams, C.F.F.Karney, Phys.Fluids **B1**, 1355 (1989).

[8] V.Krivenski, I.Fidone, G.Giruzzi, G.Granata, R.L.Meyer, E.Mazzucato, Nucl.Fusion **25** (1985) 127.

[9] M.Taguchi, Plasma Phys. Contr. Fusion **31**, 241 (1989).

[10] C.F.F.Karney, Comp. Phys. Reports **4**, 183 (1986).

This is a blank page.

国際単位系 (SI) と換算表

表 1　SI基本単位および補助単位

量	名称	記号
長さ	メートル	m
質量	キログラム	kg
時間	秒	s
電流	アンペア	A
熱力学温度	ケルビン	K
物質量	モル	mol
光度	カンデラ	cd
平面角	ラジアン	rad
立体角	ステラジアン	sr

表 2　SIと併用される単位

名称	記号
分，時，日	min，h，d
度，分，秒	°，′，″
リットル	l，L
トン	t
電子ボルト	eV
原子質量単位	u

1 eV = 1.60218 × 10^{-19} J

1 u = 1.66054 × 10^{-27} kg

表 5　SI接頭語

倍数	接頭語	記号
10^{18}	エクサ	E
10^{15}	ペタ	P
10^{12}	テラ	T
10^{9}	ギガ	G
10^{6}	メガ	M
10^{3}	キロ	k
10^{2}	ヘクト	h
10^{1}	デカ	da
10^{-1}	デシ	d
10^{-2}	センチ	c
10^{-3}	ミリ	m
10^{-6}	マイクロ	μ
10^{-9}	ナノ	n
10^{-12}	ピコ	p
10^{-15}	フェムト	f
10^{-18}	アト	a

表 3　固有の名称をもつSI組立単位

量	名称	記号	他のSI単位による表現
周波数	ヘルツ	Hz	s^{-1}
力	ニュートン	N	$m \cdot kg/s^2$
圧力，応力	パスカル	Pa	N/m^2
エネルギー，仕事，熱量	ジュール	J	N·m
工率，放射束	ワット	W	J/s
電気量，電荷	クーロン	C	A·s
電位，電圧，起電力	ボルト	V	W/A
静電容量	ファラド	F	C/V
電気抵抗	オーム	Ω	V/A
コンダクタンス	ジーメンス	S	A/V
磁束	ウェーバ	Wb	V·s
磁束密度	テスラ	T	Wb/m^2
インダクタンス	ヘンリー	H	Wb/A
セルシウス温度	セルシウス度	℃	
光束	ルーメン	lm	cd·sr
照度	ルクス	lx	lm/m^2
放射能	ベクレル	Bq	s^{-1}
吸収線量	グレイ	Gy	J/kg
線量当量	シーベルト	Sv	J/kg

表 4　SIと共に暫定的に維持される単位

名称	記号
オングストローム	Å
バーン	b
バール	bar
ガル	Gal
キュリー	Ci
レントゲン	R
ラド	rad
レム	rem

1 Å = 0.1 nm = 10^{-10} m

1 b = 100 fm^2 = 10^{-28} m^2

1 bar = 0.1 MPa = 10^5 Pa

1 Gal = 1 cm/s^2 = 10^{-2} m/s^2

1 Ci = 3.7 × 10^{10} Bq

1 R = 2.58 × 10^{-4} C/kg

1 rad = 1 cGy = 10^{-2} Gy

1 rem = 1 cSv = 10^{-2} Sv

（注）

1. 表1－5は「国際単位系」第5版，国際度量衡局 1985年刊行による。ただし，1 eVおよび1 uの値はCODATAの1986年推奨値によった。
2. 表4には海里，ノット，アール，ヘクタールも含まれているが日常の単位なのでここでは省略した。
3. barは，JISでは流体の圧力を表わす場合に限り表2のカテゴリーに分類されている。
4. EC閣僚理事会指令ではbar，barnおよび「血圧の単位」mmHgを表2のカテゴリーに入れている。

換算表

力	N(=10^5 dyn)	kgf	lbf
	1	0.101972	0.224809
	9.80665	1	2.20462
	4.44822	0.453592	1

粘度　1 Pa·s(N·s/m^2) = 10 P(ポアズ)(g/(cm·s))

動粘度　1 m^2/s = 10^4 St(ストークス)(cm^2/s)

圧力	MPa(=10 bar)	kgf/cm^2	atm	mmHg(Torr)	lbf/in^2(psi)
	1	10.1972	9.86923	7.50062 × 10^3	145.038
	0.0980665	1	0.967841	735.559	14.2233
	0.101325	1.03323	1	760	14.6959
	1.33322 × 10^{-4}	1.35951 × 10^{-3}	1.31579 × 10^{-3}	1	1.93368 × 10^{-2}
	6.89476 × 10^{-3}	7.03070 × 10^{-2}	6.80460 × 10^{-2}	51.7149	1

エネルギー・仕事・熱量	J(=10^7 erg)	kgf·m	kW·h	cal(計量法)	Btu	ft·lbf	eV
	1	0.101972	2.77778 × 10^{-7}	0.238889	9.47813 × 10^{-4}	0.737562	6.24150 × 10^{18}
	9.80665	1	2.72407 × 10^{-6}	2.34270	9.29487 × 10^{-3}	7.23301	6.12082 × 10^{19}
	3.6 × 10^6	3.67098 × 10^5	1	8.59999 × 10^5	3412.13	2.65522 × 10^6	2.24694 × 10^{25}
	4.18605	0.426858	1.16279 × 10^{-6}	1	3.96759 × 10^{-3}	3.08747	2.61272 × 10^{19}
	1055.06	107.586	2.93072 × 10^{-4}	252.042	1	778.172	6.58515 × 10^{21}
	1.35582	0.138255	3.76616 × 10^{-7}	0.323890	1.28506 × 10^{-3}	1	8.46233 × 10^{18}
	1.60218 × 10^{-19}	1.63377 × 10^{-20}	4.45050 × 10^{-26}	3.82743 × 10^{-20}	1.51857 × 10^{-22}	1.18171 × 10^{-19}	1

1 cal = 4.18605 J(計量法)

= 4.184 J　(熱化学)

= 4.1855 J　(15 °C)

= 4.1868 J(国際蒸気表)

仕事率　1 PS(仏馬力)

= 75 kgf·m/s

= 735.499 W

放射能	Bq	Ci
	1	2.70270 × 10^{-11}
	3.7 × 10^{10}	1

吸収線量	Gy	rad
	1	100
	0.01	1

照射線量	C/kg	R
	1	3876
	2.58 × 10^{-4}	1

線量当量	Sv	rem
	1	100
	0.01	1

(86年12月26日現在)